IEEE Access
Multidisciplinary | Rapid Review | Open Access Journal

Received April 11, 2019, accepted April 24, 2019, date of publication April 30, 2019, date of current version May 13, 2019.

Digital Object Identifier 10.1109/ACCESS.2019.2913952

Research on Torque Characteristics of a Modular Arc-Linear Flux Switching Permanent-Magnet Motor

BIN LI[1], JING ZHAO[1], (Member, IEEE), QUANSONG MOU[1], XIANGDONG LIU[1], (Member, IEEE), A. HADDAD[2], (Member, IEEE), AND JUN LIANG[2], (Senior Member, IEEE)

[1]School of Automation, Beijing Institute of Technology, Beijing 100081, China
[2]School of Engineering, Cardiff University, Cardiff CF24 3AA, U.K.

Corresponding author: Jing Zhao (zhaojing_bit@bit.edu.cn)

This work was supported in part by the Intelligent Equipment and Technology of Automation Research and Development Platform under Grant 2016F2FC007.

ABSTRACT The modular arc-linear flux switching permanent-magnet motor (MAL-FSPM) used for scanning system is researched in this paper by the finite element method (FEM). The MAL-FSPM combines characteristics of the flux switching permanent-magnet motor and linear motor and can realize the direct driving and limited angular movement. Due to the double salient effect, the cogging torque including slot torque and end torque is very high. In order to reduce the cogging torque, a method of magnetizing the permanent magnet in reverse direction combined with rotor segmentation is proposed. By means of the proposed method, peak-peak cogging torque and load torque ripple are reduced effectively. Besides, the smooth operation range and an average load torque of the motor are also optimized. The effectiveness of the method is verified by both 2D and 3D FE models.

INDEX TERMS Modular arc-linear flux switching permanent-magnet motor, cogging torque, segment rotor, magnetization direction of permanent magnet, finite element.

I. INTRODUCTION

In many applications, such as antenna, satellite scan mirror, robot joint, etc, the driven objects only rotate back and forth within a limited angle range. The arc-linear motors are good candidates as direct driving machines for these applications to satisfy the requirements of high positioning accuracy and high response performance. Since the windings in the primary are connected to an external power supply and it is not conducive to movement, the secondary with permanent magnets (PMs) is often chosen as mover in arc-linear motor or linear motor [1]–[4]. However, different from rotary PMSM, the rotor with PMs is much longer than the stator in order to obtain a large operation range. During operation, the effective slot-pole match between stator and rotor is fixed, and the part of rotor with PMs which is not coupled with stator will be useless, even cause electromagnetic interference to external equipment.

The flux-switching PM (FSPM) machine has a series of advantages. Since the rotor core of FSPM machine is directly laminated from silicon steel sheets, its structure is simple and its mechanical strength is high [5], [6]. Since PMs are installed in the stator, FSPM motors are able to avoid the problem of permanent magnets falling off during operation [7], [8]. The magnetization direction of the adjacent permanent magnets on the stator is opposite along the circumferential direction and the stator teeth have good magnetic gathering effect which will lead to a high torque density [9], [10]. Besides, the magnetic field generated by the permanent magnet and the magnetic field generated by the armature reaction are in parallel magnetic circuit relationship, so the armature reaction has little influence on the main pole magnetic field [11], [12]. Considering the above advantages, the arc-linear FSPM motor is chosen for the research investigation in this paper.

However, the double salient effect in FSPM motors leads to a large cogging torque [13], [14]. Due to the particularity of the structure of the FSPM motors, some methods applied in conventional PMSM to decrease cogging torque,

The associate editor coordinating the review of this manuscript and approving it for publication was Xiaodong Liang.

2169-3536 © 2019 IEEE. Translations and content mining are permitted for academic research only.
Personal use is also permitted, but republication/redistribution requires IEEE permission.
See http://www.ieee.org/publications_standards/publications/rights/index.html for more information.

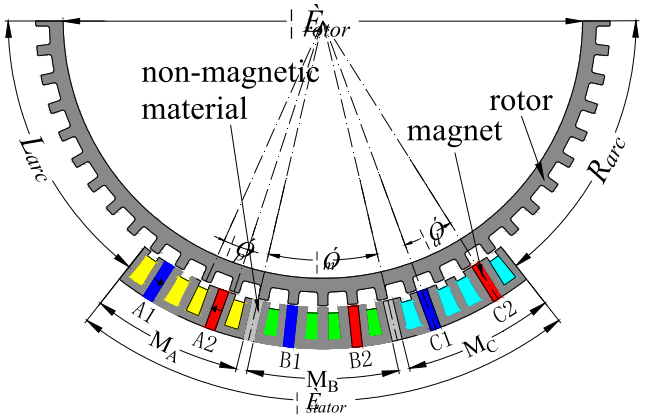

FIGURE 1. The structure of the MAL-FSPM.

such as PM pole arc-embrace, magnet segmentation, slot skewing, and slot opening shift are not easily realized for FSPM motors. There are many methods to reduce the cogging torque, such as rotor tooth with odd number [14], multi-tooth structure [15], [16], rotor tooth shapes combined with stepped and notched technology [17], [18]. But these methods require large amount of calculation and complex optimization and may not be suitable for modular motors. On the other hand, the limited stator length of the linear motor can cause end effects, which cause unbalanced back EMF and a large cogging torque. Adjusting auxiliary tooth, auxiliary tooth with auxiliary magnets, optimization of ratio of stator width to rotor width, modular primaries and adding damping system to the end can reduce the cogging torque or cogging force [19]–[27]. However, end effects influence with rotor end meeting the stator end is not considered. This paper proposes a method that considers the normal case and the special case (rotor end meets stator end) for reducing the cogging torque. Moreover, the method can provide a perfect balanced back EMF.

Firstly, the initial structure of a modular arc-linear flux switching permanent-magnet motor (MAL-FSPM) is introduced in section II. Secondly, a novel cogging torque reduction method is introduced in section III. Thirdly, the FEM results that include the flux linkage, back EMF, cogging torque and load torque are obtained to verify the method in section IV. Then, the scan range and average load torque are optimized in section V.

II. THE STRUCTURE OF CONVENTIONAL MAL-FSPM

As shown in Fig. 1(a), MAL-FSPM can be seen as a part of rotary modular FSPM. The effective slot/pole combination of the MAL-FSPM in this paper is 12-slots/13-poles [28]. The structure of the rotor is simple, just laminated from silicon steel sheets. The rotor teeth pitch τ_p is 6° and the arc radian of rotor θ_{rotor} is 180°. τ_p and θ_{rotor} are expressed in mechanical angle and so are the following variables related to angle. The stator of MAL-FSPM is composed of three modules (M_A, M_B, and M_C) and magnetic isolation blocks are installed between any two adjacent modules. Each module

TABLE 1. The main dimension parameters of each module.

Symbol	Machine Parameters	Values
H_{th}	Height of rotor tooth (mm)	5
L_a	Length of the motor (mm)	65
D_{SOut}	Outer diameter of stator (mm)	240
δ	Length of air-gap (mm)	0.75
W_{rt}	Width of rotor tooth (°)	2
τ_p	Pitch of rotor tooth (°)	6
W_{pm}	Thickness of magnet (°)	2
h_{pm}	Height of magnet (mm)	15
W_M	Width of each module (°)	24
W_b	Width of non-magnetic block in circumferential direction (°)	2
$W_{non\text{-}mag}$	Width of non-magnetic block in radial direction (mm)	2
W_{slot}	Width of slot (°)	2
W_{Ust}	Tooth width of 'U' type (°)	1.5
W_{Est}	Tooth width of 'E' type (°)	2
m	Phase number	3
n	Rated speed (r/min)	100
I_N	Amplitude of phase current (A)	2.26

is composed of an 'E' shape iron core, two 'U' shape iron cores, two PMs with opposite magnetization direction and two coils belonging to the same phase. Magnetic isolation blocks are made of non-magnetic material. The arc radian of stator θ_{stator} is 76° and the corresponding right scanning range R_{arc} and left scanning range L_{arc} of the motor are both 52°.

The electric period of FSPM motors is a rotor teeth pitch τ_p [16]–[18]. For a three-phase motor, in order to obtain balanced three-phase back-EMF, the phase difference between adjacent phase modules τ_m should be 120° (electrical degree). That is τ_m should satisfies equation (1). Besides, in order to obtain the maximum back EMF of a single phase, the winding factor should be 1 or close to 1. Thus, the distance between two PMs with opposite magnetization directions in the same module τ_d should satisfies equation (2).

$$\tau_m = \left(j + \frac{2^k}{3}\right) \times \tau_p \tag{1}$$

$$\tau_d = \left(i + \frac{1}{2^k}\right) \times \tau_p \tag{2}$$

where the value of k is 0 or 1, i and j are both nonnegative integer. In this paper, k is 0, i is 1 and j is 4.

The dimensions of the module parameters are shown in Table I.

III. NOVEL METHOD OF COGGING TORQUE REDUCTION

In the arc-linear FSPM motor, the cogging torque consists of slot effect torque and end effect torque. The slot effect torque is similar to that in general rotary FSPM motors. Due to the double salient effect of the FSPM motor, the magnetic reluctance in the motor is nonuniform. In the no-load condition, the rotor always tries to move to the position where the

magnetic reluctance is the smallest and will produce a no-load slot effect torque. The slot effect torque will change with the rotor position and produce cogging torque fluctuation. Besides, due to the stator length being limited in arc-linear motor, the left and right ends of the stator will interact with the rotor separately and will produce an end torque. In MAL-FSPM motors, the rotor will be affected by these two factors and will try to move to the position with the smallest magnetic reluctance.

The back EMF can be calculated as follows:

$$e = \frac{d\psi_m}{dt} = \frac{d\psi_m}{d\alpha} \cdot \frac{d\alpha}{dt} = \omega_r \frac{d\psi_m}{d\alpha} \tag{3}$$

where ψ_m is the flux linkage of phase winding, e is the back EMF, t is time, α is the mechanical rotor position, and ω_r is the mechanical rotating speed.

According to the above analysis, the cogging torque and back EMF are related to the rotor position and can be expressed as (4) and (5).

$$T_{cog} = -\frac{\partial W(\alpha)}{\partial \alpha} = \sum_{i=1}^{\infty} \left[T_{cog,v} \sin(v \frac{2\pi}{\tau_p} \alpha + \theta_{cog,v}) \right] \tag{4}$$

$$\begin{aligned} e &= \frac{d\psi_m}{dt} = \frac{d\psi_m}{d\alpha} \cdot \frac{d\alpha}{dt} = \omega_r \frac{d\psi_m}{d\alpha} \\ &= \sum_{v=1}^{\infty} \left[e_v \sin(v \frac{2\pi}{\tau_p} \alpha + \theta_{e,v}) \right] \end{aligned} \tag{5}$$

where $T_{cog,v}$ is the vth harmonic amplitude in cogging torque, $\theta_{cog,v}$ is the vth harmonic phase in cogging torque, W is magnetic field energy, e_v is the vth harmonic amplitude in back EMF, $\theta_{e,v}$ is the vth harmonic phase.

The initial position of the rotor can influence the phase of the cogging torque and back EMF, but the initial position of the rotor can not change the amplitude of the cogging torque and back EMF [13]. As for the MAL-FSPM, the magnetic field changes periodically with the period of one rotor tooth (τ_p), so the back EMF and the cogging torque also change with the period of one rotor tooth. Therefore, if the rotor of the MAL-FSPM is divided into two segments with angular difference θ_x (mechanical angle), the cogging torque and back EMF can be expressed as (6) and (7).

$$\begin{aligned} T_{cog} = \frac{1}{2} \sum_{v=1}^{\infty} \Bigg[& T_{cog,v} \sin(v \frac{2\pi}{\tau_p} (\alpha + \theta_x) + \theta_{cog,v}) \\ & + T_{cog,v} \sin(v \frac{2\pi}{\tau_p} \alpha + \theta_{cog,v}) \Bigg] \end{aligned} \tag{6}$$

$$\begin{aligned} e = \frac{1}{2} \sum_{v=1}^{\infty} \Bigg[& e_v \sin(v \frac{2\pi}{\tau_p} (\alpha + \theta_x) + \theta_{e,v}) \\ & + e_v \sin(v \frac{2\pi}{\tau_p} \alpha + \theta_{e,v}) \Bigg] \end{aligned} \tag{7}$$

It can be found, if $\theta_x = \tau_p/2$ (mechanical angle), the cogging torque can be removed completely. However, when the cogging torque is removed, the back EMF is also removed and the output torque will be correspondingly removed.

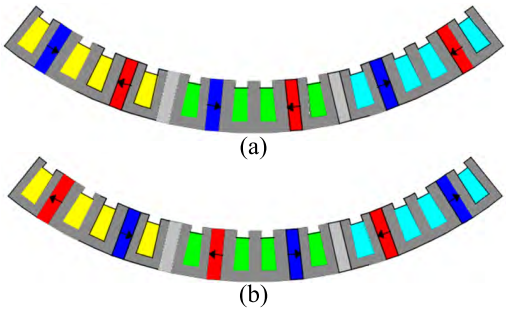

FIGURE 2. Magnetization scheme: (a) magnetization scheme A; (b). magnetization scheme B.

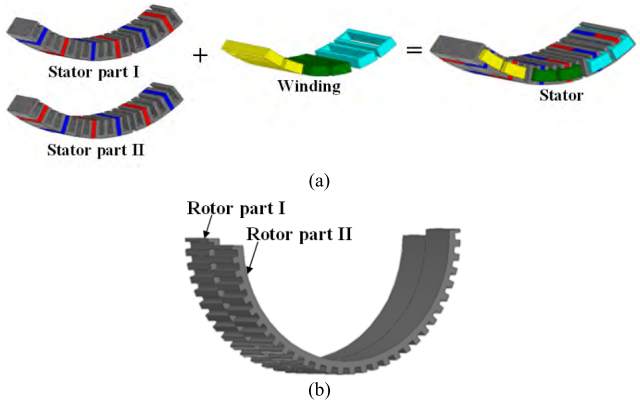

FIGURE 3. Establishment of stator and rotor (a). Stator part. (b). Rotor part.

It is well known that the field energy W is a scalar physical quantity and while the flux linkage ψ_m is vector physical quantity. If rotor position remains identical, the cogging torque is the same for the magnetization scheme A and magnetization scheme B, as shown in the Fig. 2, where the magnets are colored with blue or red in the stator. The magnetization directions of the blue magnets and red magnets are opposite in the circumference direction. However, the phase angle of the back EMFs for the magnetization scheme A and magnetization scheme B are opposite.

Therefore, combining the two aforementioned important characteristics, the cogging torque can be removed without influencing the back EMF and output torque by magnetizing the permanent magnet in the reverse direction combined with rotor step skewing.

The stator and rotor structure are shown as Fig. 3. The stator consists of stator part I with magnetization scheme A, stator part II with magnetization scheme B and windings. There is no angular difference between stator part I and stator part II. As for rotor part, an angular difference ($\tau_p/2 = 3°$) exists between rotor part I and rotor part II. Rotor part I corresponds to stator part I, and rotor part II corresponds to stator part II.

IV. THE FEM RESULTS

In order to verify the effect of proposed method, 2D and 3D FE models are established and simulated. For the convenience of description, combination of stator part I and rotor part I

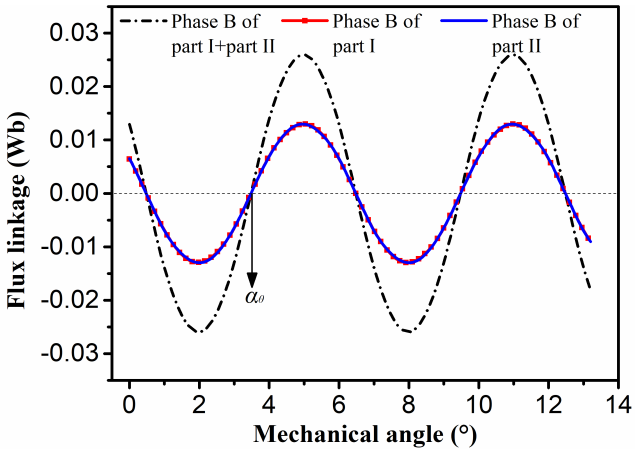

FIGURE 4. Flux linkage of phase B.

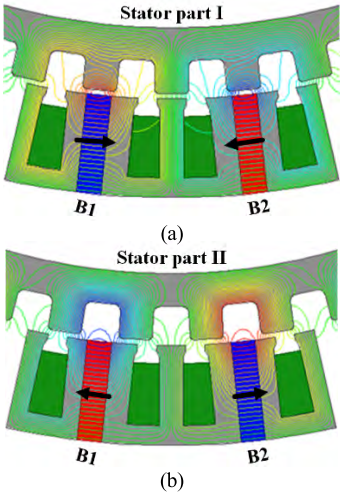

FIGURE 5. Flux distribution of module M_B at rotor position α_θ (a). Part I. (b) Part II.

represent part I, and combination of stator part II and rotor part II represent part II.

A. THE FLUX LINKAGE

The flux linkage of phase B is shown as Fig. 4 and flux distribution of rotor position α_θ for module M_B is shown in Fig. 5. According to Fig. 4 and Fig. 5, although the magnetization direction of magnet wound by the coil B1 is opposite in the circumference direction, the flux linkage of coil B1 is in agreement and changes simultaneously from maximum value to minimum value with the period of 6°.

B. THE BACK EMF

The back EMFs for phase B of part I, phase B of part II, phase A, phase B and phase C are shown in Fig. 6. According to Fig. 6, the period of the back EMF is one rotor tooth of 6°. Taking phase B as an example, the back EMF of phase B for Part I and Part II are in good agreement. In addition, the three phases back EMFs have almost the same amplitude, which indicate that the three phase back EMFs are well balanced. Table II shows the maximum value, the minimum value and

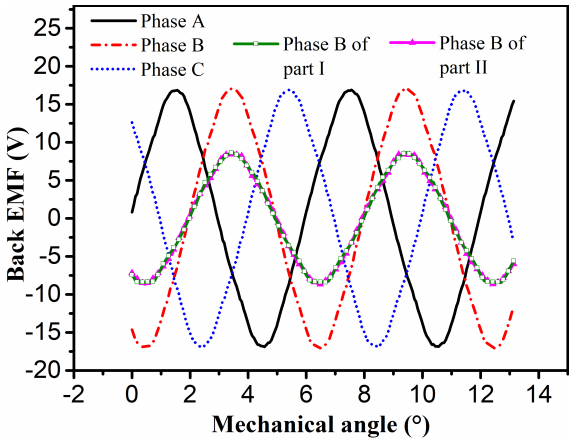

FIGURE 6. Back EMF of the proposed motor.

TABLE 2. The characteristics of the back EMF.

Parameters	Maximum (V)	Minimum (V)	THD (%)
Phase B of part I	8.4	-8.7	4.23
Phase B of part II	8.7	-8.4	4.31
Phase B	17.1	-17.1	3.39

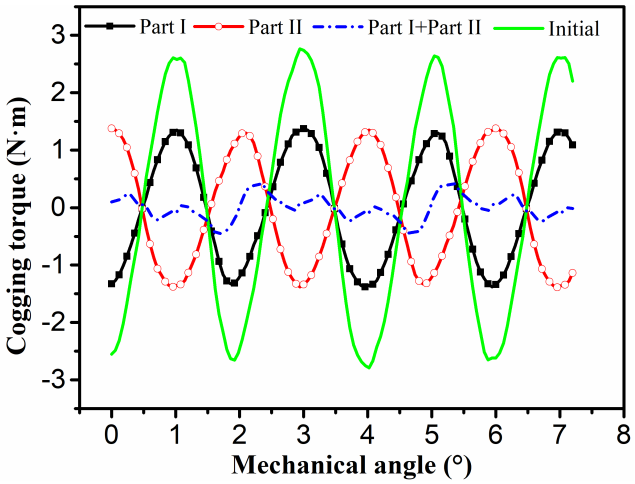

FIGURE 7. Cogging torque in the condition of $d_{end} > \tau_p$.

the total harmonic distortion (THD) of the back EMF. The THD of phase B is smaller than that of Part I and Part II. Therefore, after the superposition of phase back EMF of Part I and Part II, the THD has improved significantly. Therefore, the back EMF verifies the aforesaid analysis and method.

C. COOGING TORQUE

Define the distance between the left end of the rotor and the left end of the stator, or the distance between the right end of the rotor and the right end of the stator as d_{end}. When d_{end} is more than one rotor tooth pitch τ_p, the cogging torque of the initial structure, stator part I, stator part II, and part I+ part II is shown as Fig. 7. It can be seen that the cogging torque curves of stator part I and stator part II have the opposite phase angles. Consequently, the cogging torque can be cancelled out as much as possible by the combination of part I and part II.

TABLE 3. The characteristics of cogging torque ($d_{end} > \tau_p$).

Parameters	Maximum (N•m)	Minimum (N•m)	Peak-peak (N•m)
Initial	2.76	-2.79	5.56
Part I	1.38	-1.39	2.77
Part II	1.38	-1.39	2.77
Part I+ Part II	0.48	-0.54	1.02

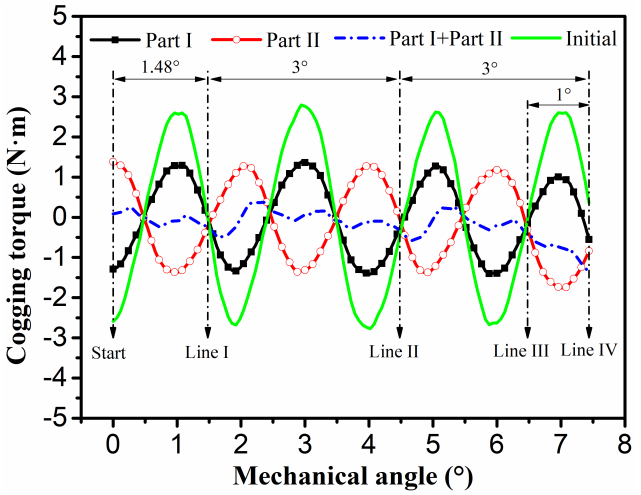

FIGURE 8. Cogging torque in the condition of $\tau_p > d_{end} > 0°$.

Compared with the initial structure, the peak-peak value of the cogging torque is reduced from 5.56N·m to 1.02N·m, equivalent to 78.4%. Table 3 shows maximum, minimum and peak-peak value of cogging torque when $d_{end} > \tau_p$.

When the rotor end is close to the stator end, two cases are included: (1) left end of rotor meets left end of stator; (2) right end of rotor meets right end of stator. Due to the symmetry of the two cases, only the first case is researched. When the distance between the left end of the rotor and the left end of the stator (d_{end}) is less than one rotor tooth pitch, the cogging torque curves are shown as Fig. 8. As can be seen from Fig. 8, the negative amplitude of the part II curve increases when $1° > d_{end} > 0°$, that is the rotor position is between Line III and Line IV, but the part I curve basically remains unchanged. This is because an angular difference of $\tau_p/2(3°)$ exists between rotor part I and rotor part II, and rotor part I has end teeth. The end magnetic field of rotor part II will be distorted because rotor part II does not have end teeth. Nevertheless, compared with the initial structure, the end effect can be effectively reduced by the superposition of part I and part II when the rotor end meets the stator end. Table 4 shows the comparison of characteristics of cogging torque between the initial structure and the proposed structure when $\tau_p > d_{end} > 0°$.

D. LOAD TORQUE

Corresponding to Fig. 8, when $\tau_p > d_{end} > 0°$, the load torque curves are shown as Fig. 9. Due to the angular difference of $\tau_p/2$ (3°) between rotor part I and rotor part II and because rotor part II does not have end teeth, the torque ripple is a little bigger between Line III and Line IV than

TABLE 4. The characteristics of cogging torque ($\tau_p > d_{end} > 0°$).

Parameters	Range of d_{end}	Maximum	Minimum	Peak-peak
Initial	(1°, τ_p)	2.75 N·m	-2.83 N·m	5.58 N·m
	(0°, τ_p)	2.75 N·m	-2.83 N·m	5.58 N·m
Part I+ Part II	(1°, τ_p)	0.36 N·m	-0.50 N·m	0.86 N·m
	(0°, τ_p)	0.36 N·m	-1.53 N·m	1.89 N·m

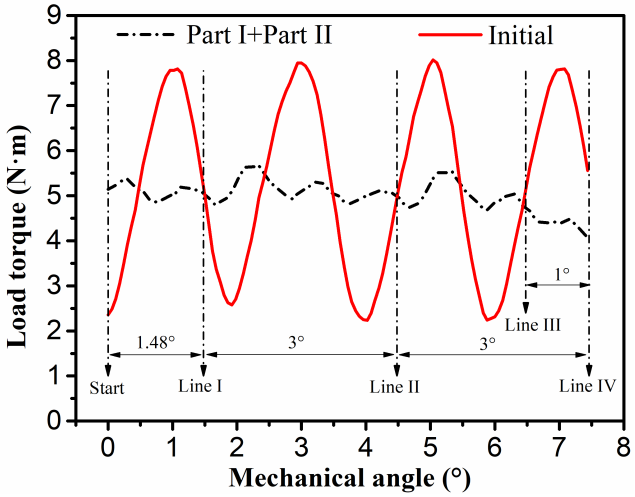

FIGURE 9. Load torque in the condition of $\tau_p > d_{end} > 0°$.

TABLE 5. The characteristics of load torque ($\tau_p > d_{end} > 0°$).

Parameters	Range of d_{end}	Peak-peak	Average	Torque ripplr
Initial	(1°, τ_p)	5.85 N·m	5.00 N·m	58.5%
	(0°, τ_p)	5.85 N·m	5.12 N·m	57.1%
Part I+ Part II	(1°, τ_p)	0.80 N·m	5.13 N·m	7.8%
	(0°, τ_p)	1.72 N·m	5.05 N·m	17.0%

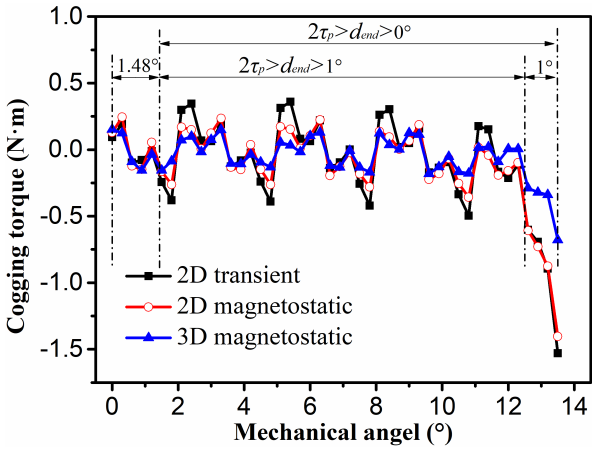

FIGURE 10. Cogging torque verified by 3D FE model.

that of between Line I and Line III. Compared with the initial structure, the torque ripple improved greatly. The torque ripple reduced from 58.6% to 7.8% (by 86.7%) when $\tau_p > d_{end} > 1°$. The torque ripple reduced from 57.1% to 17.0% (by 70.2%) when $\tau_p > d_{end} > 0°$. Table 5 shows the comparison of characteristics of load torque between initial structure and proposed structure when $\tau_p > d_{end} > 0°$.

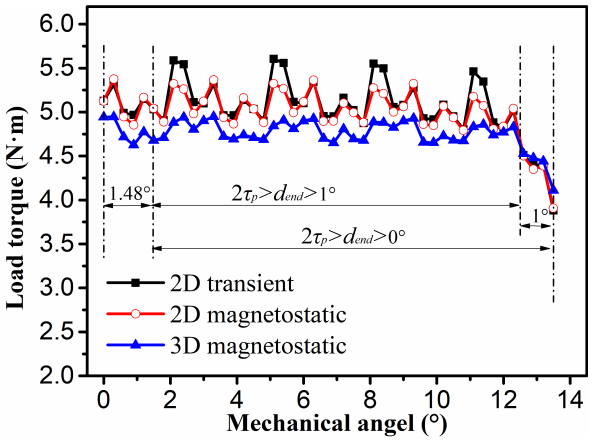

FIGURE 11. Load torque verified by 3D FE model.

TABLE 6. The characteristics of torque ($2\tau_p > d_{md} > 1°$).

Parameters	2D transient	2D magnetostatic	3D magnetostatic
Peak-peak value of cogging torque	0.86 N·m	0.59 N·m	0.33 N·m
Peak-peak value of load torque	0.80 N·m	0.58 N·m	0.30 N·m
Average value of load torque	5.13 N·m	5.05 N·m	4.79 N·m
Load torque ripple	7.8%	5.7%	3.1%

E. 3D FEM VERIFICATION

Based on Fig. 3, a 3D magnetostatic FEM simulation model is established and compared with the 2D transient model and the 2D magnetostatic model. The cogging torque and load torque waveforms of 2D transient, 2D magnetostatic and 3D magnetostatic are shown in Fig. 10 and Fig. 11for $2\tau_p > d_{end} > 0°$. Table 6 and Table 7 show peak-peak values of the cogging torque, peak-peak values of the load torque, average values of the load torque and the torque ripple in detail. The characteristics of torque when $2\tau_p > d_{end} > 1°$ are shown in Table 6 and the characteristics of torque when $2\tau_p > d_{end} > 0°$ are shown in Table 7.

As shown in Fig. 10, the waveforms of the cogging torque of 2D transient model, 2D magnetostatic model and 3D magnetostatic model are basically consistent. As shown in Fig. 11, the waveforms of load torque of 2D transient model and 2D magnetostatic model are basically consistent, but the load torque of 3D magnetostatic model is a little smaller than that of 2D models. The main reason is that there exists interpole flux leakage between permanent magnets corresponding to stator part I and stator part II in the axial direction, while 2D FEM model ignores this kind of flux leakage and makes the load torque larger. Besides, it is clear that the torque ripple during $1° > d_{end} > 0°$ is much larger than that during $2\tau_p > d_{end} > 1°$. According to Fig. 10, Fig. 11, Table 6 and Table 7, the peak-peak value of the cogging torque and load torque ripple when $1° > d_{end} > 0°$ in 3D magnetostatic model are slightly smaller than these in 2D FE models. The reason may be that the end effect in the 3D FE model can improve the magnetic field distortion caused by the stator end and rotor end close to each other. Nevertheless, the 3D magnetostatic results verify the effectiveness of the permanent magnet reversed magnetization combined with the rotor segmentation method in eliminating the cogging torque and load torque ripple.

TABLE 7. The characteristics of torque ($2\tau_p > d_{end} > 0°$).

Parameters	2D transient	2D magnetostatic	3D magnetostatic
Peak-peak value of cogging torque	1.89 N·m	1.64 N·m	0.83 N·m
Peak-peak value of load torque	1.72 N·m	1.46 N·m	0.84 N·m
Average value of load torque	5.05 N·m	4.97 N·m	4.75 N·m
Load torque ripple	17.0%	14.6%	8.8%

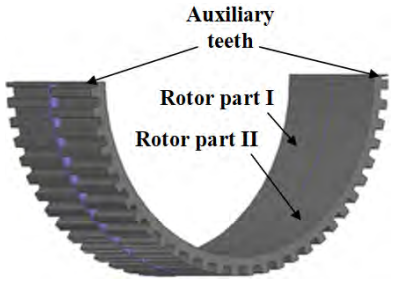

FIGURE 12. Auxiliary teeth added to rotor part II.

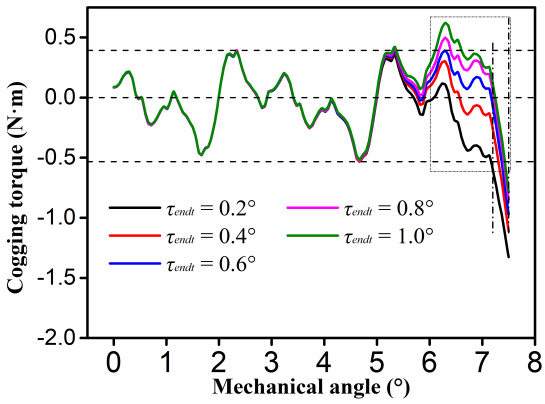

FIGURE 13. Relationship between cogging torque and auxiliary teeth width τ_{endt}.

Furthermore, if the left scan range (θ_L) and right scan range (θ_R) of the motor are reduced to 51° respectively (i.e. reduce 1°), that is ignore the operating range of $1° > d_{end} > 0°$with large fluctuation, the torque fluctuation in the whole operation range will be less than 7.8%.

V. SCAN RANGE AND AVERAGE LOAD TORQUE OPTIMIZATION

A. SCAN RANGE OPTIMIZATION

Because rotor part II has no end teeth, when the distance between stator and rotor end is between 0° and 1°, the cogging torque and load torque ripple is the largest. If the motor is wanted to run smoothly in the whole operating range, it is necessary to reduce the left and right scanning range. In order to minimize the range with large torque fluctuation,

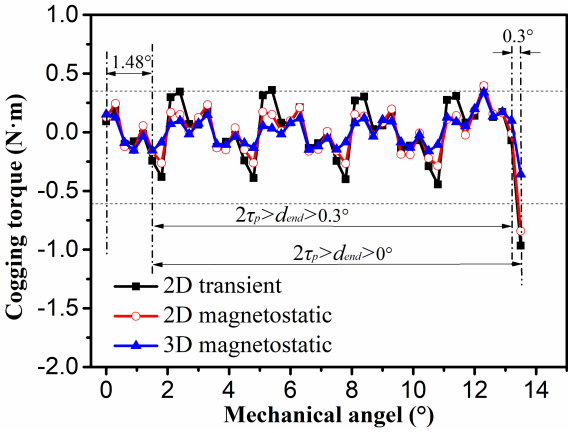

FIGURE 14. Cogging torque when $\tau_{endt} = 0.6°$.

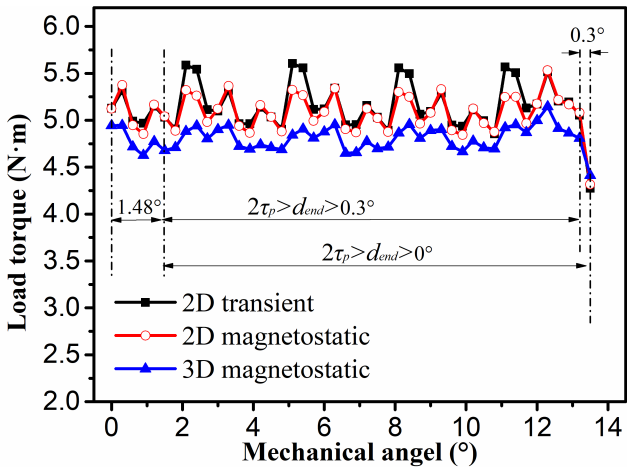

FIGURE 15. Load torque when $\tau_{endt} = 0.6°$.

auxiliary teeth are symmetrically added at the left and right ends of rotor part II, as shown in Fig. 12. The width of the auxiliary teeth τ_{endt} is optimized. The range of τ_{endt} is $0.2° \sim 1.0°$, and the change step is 0.2°. When $\tau_p > d_{end} > 0°$, the relationship between the cogging torque and auxiliary teeth width τ_{endt} is shown in Fig. 13. With the increase of τ_{endt}, the cogging torque waveform tends to move upward when the rotor end approaches the stator end (part of dotted box in Fig. 13). The up-line and down-line in Fig. 13 are the maximum and minimum values of the cogging torque when the stator end and rotor end are far apart from each other. The two lines are used to evaluate the cogging torque waveform when $\tau_p > d_{end} > 0°$. In order to make the cogging torque waveforms between the two lines as much as possible, τ_{endt} is taken as 0.6°.

When τ_{endt} is 0.6°, the FE models of 2D magnetostatic, 2D transien and 3D magnetostatic are established. The cogging torque and load torque curves are shown in Fig. 14 and Fig. 15 respectively. As can be seen in Fig. 14 and Fig. 15, the cogging torque and load torque curves have good agreement. Compared with Fig. 15 and Fig. 11, the range with a large torque fluctuation is decreased from $1° > d_{end} > 0°$ to $0.3° > d_{end} > 0°$ after adding auxiliary teeth, which decreases by 70%.

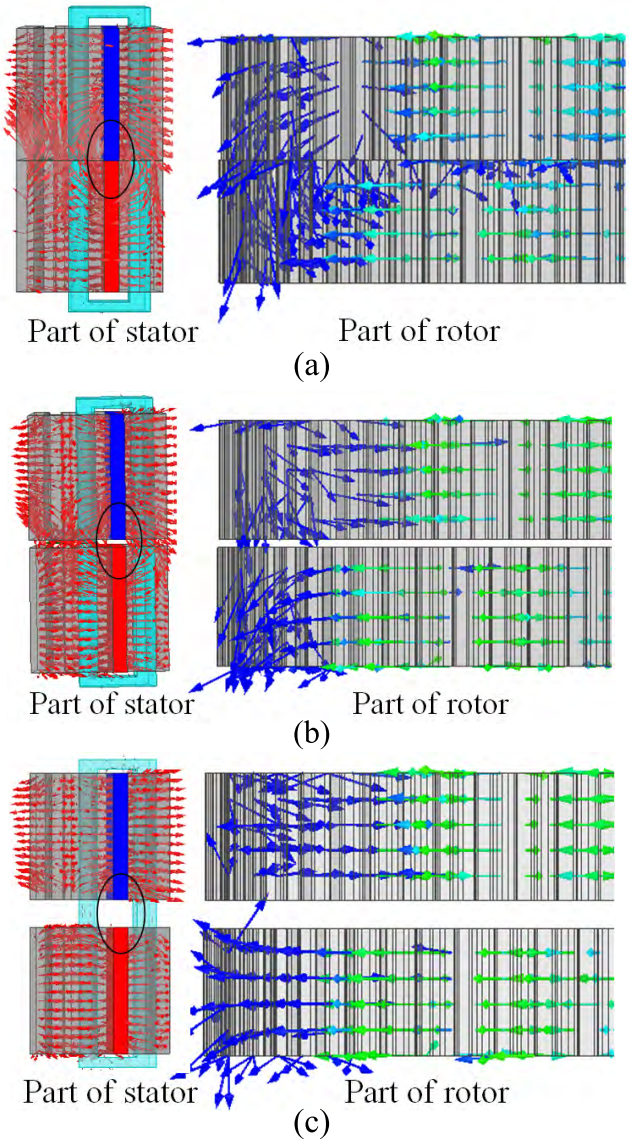

FIGURE 16. Comparison of magnetic density vector distribution with different $W_{non-mag}$. (a). No non-magnetic block. (b). $W_{non-mag}$ is 2mm. (c). $W_{non-mag}$ is 7mm.

B. AVERAGE LOAD TORQUE OPTIMIZATION

As aforementioned analysis, the average load torque in the 3D FE model is a little smaller than that in the 2D FE model which may be caused by interpole flux leakage. As shown in the black ellipse in Fig. 16 (a), there is self-closing flux at the connection of two PMs, which is not coupled with any coil and becomes flux leakage. When the amount of PM is fixed, this part flux leakage will reduce the effective flux coupled with the armature winding, resulting in the decrease of the average load torque. The problem of interpole flux leakage can be improved by adjusting the width of non-magnetic block $W_{non-mag}$ between part I and part II. Fig.16 shows the magnetic density vector distribution with different $W_{non-mag}$.

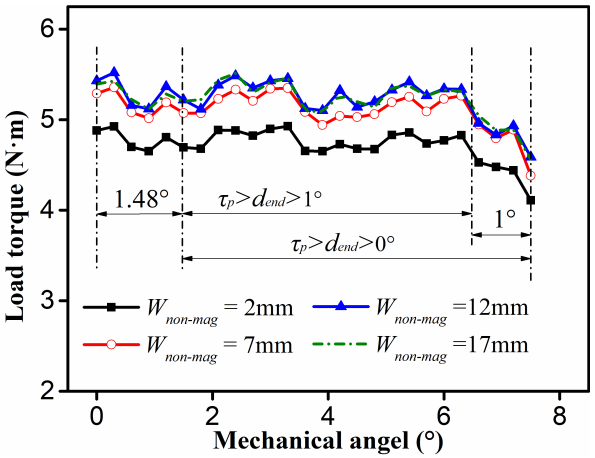

FIGURE 17. Relationship between load torque and $W_{non-mag}$.

TABLE 8. Relationship between load torque and $W_{non-mag}$ ($d_{end} > 1°$).

Parameters	2mm	7mm	12mm	17mm
Average value of load torque	4.79 N·m	5.17 N·m	5.30 N·m	5.29 N·m
Load torque ripple	3.1%	4.0%	4.0%	4.0

As clearly shown in Fig.16, the flux leakage between two parts of stator is much more serious than that between two parts of rotor. This is because there is no magnetomotive force source in the rotor and the width of non-magnetic block between two parts of rotor just needs to keep consistent to that between two parts of stator. In addition, as shown in Fig.16, with the increase of $W_{non-mag}$, the interpole flux leakage decreases correspondingly. Thus, the average load torque can also be improved correspondingly. Fig. 17 shows the relationship between load torque and $W_{non-mag}$ in 3D magetostatic FE model. Table 8 shows the corresponding load torque characteristics in detail. According to Fig. 16, Fig. 17 and Table 8, increasing $W_{non-mag}$ can reduce the influence of flux leakage on the output torque. When $W_{non-mag}$ is 7 mm, the output torque is equivalent to that of the initial structure shown in Fig. 1. When $W_{non-mag}$ is larger than 12 mm, increasing $W_{non-mag}$ has almost no effect on the average load torque. With the increase of $W_{non-mag}$, the volume of the machine is also increased. So the choice of $W_{non-mag}$ is followed the compromise principle: the interpole flux leakage is effectively decreased and the average load torque is effectively increased, but with the volume of the machine increasing as few as possible.

VI. CONCLUSION

This paper researches a method of reducing the cogging torque by permanent magnet reversed magnetization combined with rotor segment in detail. Based on the proposed method, a new modular arc-linear flux-switching permanent magnet motor is constructed based on 2D FEM. The flux linkage, back-EMF, cogging torque and load torque of the proposed motor are analyzed. It is found that the THD of the back-EMF is only 3.4%. Whether $\tau_p > d_{end} > 1°$ or $\tau_p > d_{end} > 0°$, the cogging torque and torque ripple are greatly reduced, but the torque ripple is larger in $1° > d_{end} > 0°$. The results of 2D FE analysis are verified by 3D FE model. The 2D and 3D FE analysis results prove the effectiveness of the proposed method. Then, end teeth are added to the part of rotor without end teeth and the width of end teeth is optimized. In this way, the range of large torque fluctuation is decreased to $0.3° > d_{end} > 0°$. Finally, the width of the non-magnetic block between part I and part II is optimized and this will overcome the problem of reducing the output torque while reducing the cogging torque. In summary, the method adopted in this paper can reduce the cogging torque and torque ripple in arc-linear FSPM motors while keeping the average torque unreduced.

REFERENCES

[1] C. Bianchini, F. Immovilli, A. Bellini, and P. Mignano, "Arc linear motors for direct drive robots: Galileo sphere," in *Proc. Ind. Appl. Soc. Annu. Meeting*, Edmonton, AB, Canada, Oct. 2008, pp. 1–7.

[2] F. Leonardi, M. Venturini, and A. Vismara, "PM motors for direct driving optical telescope," *IEEE Ind. Appl. Mag.*, vol. 2, no. 4, pp. 10–16, Jul. 1996.

[3] I. I. Abdalla, T. Ibrahim, and N. M. Nor, "Analysis of tubular linear motors for different shapes of magnets," *IEEE Access*, vol. 6, pp. 10297–10310, 2018.

[4] B. Li, J. Zhao, X. Liu, Y. Guo, H. Hu, and J. Li, "Detent force reduction of an arc-linear permanent-magnet synchronous motor by using compensation windings," *IEEE Trans. Ind. Electron.*, vol. 64, no. 4, pp. 3001–3011, Apr. 2017.

[5] W. Hua, Z. Q. Zhu, M. Cheng, Y. Pang, and D. Howe, "Comparison of flux-switching and doubly-salient permanent magnet brushless machines," in *Pro. 8th ICEMS*, Nanjing, China, Sep. 2005, pp. 165–170.

[6] W. Hua, M. Cheng, Z. Q. Zhu, and D. Howe, "Analysis and optimization of back EMF waveform of a flux-switching permanent magnet motor," *IEEE Trans. Energy Convers.*, vol. 23, no. 3, pp. 727–733, Sep. 2008.

[7] W. Zhao, M. Cheng, W. Hua, H. Jia, and R. Cao, "Back-EMF harmonic analysis and fault-tolerant control of flux-switching permanent-magnet machine with redundancy," *IEEE Trans. Ind. Electron.*, vol. 58, no. 5, pp. 1926–1935, May 2011.

[8] Z. Q. Zhu and J. T. Chen, "Advanced flux-switching permanent magnet brushless machines," *IEEE Trans. Magn.*, vol. 46, no. 6, pp. 1447–1453, Jun. 2010.

[9] J. F. Bangura, "Design of high-power density and relatively high-efficiency flux-switching motor," *IEEE Trans. Energy Convers.*, vol. 21, no. 2, pp. 416–425, Jun. 2006.

[10] E. Sulaiman, T. Kosaka, and N. Matsui, "High power density design of 6-slot-8-pole hybrid excitation flux switching machine for hybrid electric vehicles," *IEEE Trans. Magn.*, vol. 47, no. 10, pp. 4453–4456, Oct. 2011.

[11] C.-C. Hwang, C.-M. Chang, S.-S. Hung, and C.-T. Liu, "Design of high performance flux switching PM machines with concentrated windings," *IEEE Trans. Magn.*, vol. 50, no. 1, Jan. 2014, Art. no. 4002404.

[12] T. Raminosoa, C. Gerada, and M. Galea, "Design considerations for a fault-tolerant flux-switching permanent-magnet machine," *IEEE Trans. Ind. Electron.*, vol. 58, no. 7, pp. 2818–2825, Jul. 2011.

[13] X. Liu, Z. Gu, B. Li, J. Zhao, and X. Zhang, "A novel cogging torque reduction method for the modular arc-linear flux switching permanent-magnet motor," in *Proc. IEEE CEFC*, Miami, FL, USA, Nov. 2016, p. 1.

[14] J. T. Chen and Z. Q. Zhu, "Winding configurations and optimal stator and rotor pole combination of flux-switching PM brushless ac machines," *IEEE Trans. Energy Convers.*, vol. 25, no. 2, pp. 293–302, Jun. 2010.

[15] Z. Q. Zhu, J. T. Chen, Y. Pang, D. Howe, S. Iwasaki, and R. Deodhar, "Analysis of a novel multi-tooth flux-switching PM brushless AC machine for high torque direct-drive applications," *IEEE Trans. Magn.*, vol. 44, no. 11, pp. 4313–4316, Nov. 2008.

[16] J. Cai, Q. Lu, Y. Jin, C. Chen, and Y. Ye, "Performance investigation of multi-tooth flux-switching PM linear motor," in *Proc. 14th ICEMS*, Beijing, China, Aug. 2011, pp. 1–6.

[17] J. Zhao, Y. S. Yan, B. Li, X. Liu, and Z. Chen, "Influence of different rotor teeth shapes on the performance of flux switching permanent magnet machines used for electric vehicles," *Energies*, vol. 7, no. 12, pp. 8056–8075, Dec. 2014.
[18] S. E. Abdollahi and S. Vaez-Zadeh, "Reducing cogging torque in flux switching motors with segmented rotor," *IEEE Trans. Magn.*, vol. 49, no. 10, pp. 5304–5309, Oct. 2013.
[19] C. F. Wang, J. X. Shen, Y. Wang, L. L. Wang, and M. J. Jin, "A new method for reduction of detent force in permanent magnet flux-switching linear motors," *IEEE Trans. Magn.*, vol. 45, no. 6, pp. 2843–2846, Jun. 2009.
[20] H. Hu, X. Liu, J. Zhao, and Y. Guo, "Analysis and minimization of detent end force in linear permanent magnet synchronous machines," *IEEE Trans. Ind. Electron.*, vol. 65, no. 3, pp. 2475–2486, Mar. 2018.
[21] F. Xiao, X. Liu, Y. Du, K. Shi, and P. Xu, "A C-core linear flux-switching permanent magnet machine with positive additional teeth," in *Proc. 17th ICEMS*, Hangzhou, China, Oct. 2014, pp. 1757–1761.
[22] R. Cao, M. Cheng, C. Mi, W. Hua, and W. Zhao, "Comparison of complementary and modular linear flux-switching motors with different mover and stator pole pitch," *IEEE Trans. Magn.*, vol. 49, no. 4, pp. 1493–1504, Apr. 2013.
[23] X. Huang, J. Liang, B. Zhou, L. Li, and D. Gerada, "Suppressing the thrust ripple of the consequent-pole permanent magnet linear synchronous motor by two-step design," *IEEE Access*, vol. 6, pp. 32935–32944, Jun. 2018.
[24] X. Huang, Z. Qian, Q. Tan, J. Li, and B. Zhou, "Suppressing the thrust ripple of the permanent magnet linear synchronous motors with different pole structures by setting the modular primary structures differently," *IEEE Trans. Energy Convers.*, vol. 33, no. 4, pp. 1815–1824, Dec. 2018.
[25] Q. Tan, X. Huang, L. Li, and M. Wang, "Research on inductance unbalance and thrust ripple suppression of slot-less tubular permanent magnet synchronous linear motor," *IEEE Access*, vol. 6, pp. 51011–51020, 2018.
[26] Z. He, F. Dong, J. Zhao, L. Wang, J. Song, and X. Song, "Thrust ripple reduction in permanent magnet synchronous linear motor based on electromagnetic damping-spring system," *IEEE Trans. Energy Conver.*, vol. 33, no. 4, pp. 2122–2132, Dec. 2018.
[27] Z. He *et al.*, "Thrust ripple reduction in permanent magnet synchronous linear motor based on tuned viscoelastic damper," *IEEE Trans. Ind. Electron.*, vol. 66, no. 2, pp. 977–987, Feb. 2019.
[28] X. Liu, Z. Gu, and J. Zhao, "Torque ripple reduction of a novel modular arc-linear flux-switching permanent-magnet motor with rotor step skewing," *Energies*, vol. 9, no. 6, Jun. 2016, Art. no. 404.

BIN LI received the B.Sc. and M.Sc. degrees in electrical engineering from the Harbin Institute of Technology, Harbin, China, in 2005 and 2008, respectively. He is currently pursuing the Ph.D. degree with the School of Automation, Beijing Institute of Technology, Beijing, China.

His research interests include electric machines and drive systems used for industry, and special servo machine systems.

JING ZHAO (M'13) received the B.Sc. degree from the Hebei University of Technology, Tianjin, China, in 2005, and the M.Sc. and Ph.D. degrees from the Harbin Institute of Technology, Harbin, China, in 2007, and 2011, respectively, all in electrical engineering.

She is currently an Associate Professor Lecturer with the School of Automation, Beijing Institute of Technology, Beijing, China. Her research interests include electric machines and drive systems used for renewable energy, and special servo machines systems.

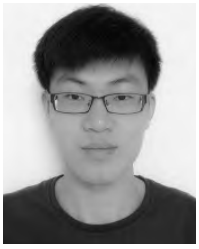

QUANSONG MOU received the B.E. degree from the School of Automation, Beijing Institute of Technology, Beijing, China, in 2017, where he is currently pursuing the M.Sc. degree with the School of Automation, Beijing Institute of Technology, Beijing, China.

His research interests include linear PM machines and new permanent magnet motor systems.

XIANGDONG LIU (M'14) was born in 1971. He received the M.S. degree in electrical engineering and the Ph.D. degree in space engineering from the Harbin Institute of Technology, Harbin, China, in 1995 and 1998, respectively.

He is currently a Professor with the School of Automation, Beijing Institute of Technology, Beijing, China. His research interests include high-precision servo control, motor drive control, piezoceramics actuator drives and compensation control, sliding control, state estimation, and attitude control.

A. HADDAD (M'13) received the first degree in electrical engineering, in 1985, and the Ph.D. degree in high voltage engineering, in 1990. He is currently a Professor with Cardiff University. His research interests are in overvoltage protection, insulation systems, insulation coordination, and earthing systems. He has published an IET-Power Series Book on the *Advances in High Voltage Engineering*. He is a member of the CIGRE working groups and a member of the BSI PEL1/2 and IEC TC37. He serves on the scientific committees of several international conferences. He is a Fellow of the IET and a Fellow of the Learned Society of Wales.

JUN LIANG (M'02–SM'12) received the B.Sc. degree from the Huazhong University of Science and Technology, Wuhan, China, in 1992, and the M.Sc. and Ph.D. degrees from the China Electric Power Research Institute, Beijing, China, in 1995 and 1998, respectively. From 1998 to 2001, he was a Senior Engineer with the China Electric Power Research Institute. From 2001 to 2005, he was a Research Associate with Imperial College, London, U.K. From 2005 to 2007, he was a Senior Lecturer with the University of Glamorgan, Wales, U.K. He is currently a Professor with the School of Engineering, Cardiff University, Wales, U.K. His research interests include power system stability and control, power electronics, and renewable power generation.